MICROCELLULAR NANOCOMPOSITE INJECTION MOLDING PROCESS

Mingjun Yuan[(1)], Lih-Sheng Turng[(1)], Rick Spindler[(2)], Daniel Caulfield[(3)], Chris Hunt [(3)]*
(1) Dept. of Mechanical Engineering, University of Wisconsin-Madison, Madison, WI 53706, USA
(2) Kaysun Corporation, Manitowoc, WI 54221, USA
(3) USDA Forest Products Laboratory, Madison, WI 53726, USA

Abstract

This study aims to explore the processing benefits and property improvements of combining nanocomposites with microcellular injection molding. The molded parts produced based on the Design of Experiments (DOE) matrices were subjected to tensile testing, impact testing, and Scanning Electron Microscope (SEM), Transmission Electron Microscope (TEM), Dynamic Mechanical Analysis (DMA), and X-ray Diffraction (XRD) analysis. Effects of processing conditions on the mechanical properties and microstructures have been studied. The results show that the supercritical fluid (N_2) helps to further exfoliate and uniformly disperse the nano-clays in the matrix during the course of molding process. Compared to the corresponding base polyamide microcellular parts, the microcellular nanocomposites exhibit better cell structures and cell distributions as well as better mechanical properties.

Introduction

Polymer-silicate nanocomposites represent a new class of high performance materials. They offer improved stiffness, heat resistance, barrier and flame retardation, and dimensional stability with a small clay load (<10%). However, polymer nanocomposite is still economically unfavorable compared to conventional polymeric materials.

In microcellular injection molding, "supercritical" nitrogen or carbon dioxide is injected into the machine barrel to create a single-phased polymer-gas solution. It is capable of producing parts with a microcellular structure (microcells of 1 to 100 microns) while using lower injection pressure, shorter cycle time, and less material. It eliminates the need of packing pressure, and improves the dimensional stability of the molded parts. Microcells also greatly enhance the part toughness of many polymeric materials by acting as crack arrestors.

Previous studies have shown that the addition of the nano-clay fillers greatly increases the viscosity of the polymer [1]. On the other hand, blending supercritical gas into polymer melt effectively reduces the viscosity and the glass transition temperature of the polymer melt, as well as the interfacial tension [2]. Hence, adding supercritical gas into the nanocomposites renders a method to tailor the rheological and surface properties of the polymer to facilitate better microcell formation and improved mechanical properties. The batch process of microcellular nanocomposite has been reported [3]. But development of continuous or semi-continuous microcellular nanocomposite processes such as injection molding on the industrial scale is more appealing considering the property-to-cost ratio and broader applications.

Experiments

Materials and experimental designs

Three different types of base polyamide resins (B, D, F) and their corresponding nanocomposite counterparts (polyamide-clay nanocomposite A, C, E) were injection molded using a 150-ton injection-molding machine equipped with microcellular injection molding capability (MuCell process). The experiments were first executed based on the L16 orthogonal array fractional factorial design. After screening the experimental parameters, the L9 orthogonal array (Table 1) design was then used in order to increase the precision of experiments. The L9 experiments contain four different operation variables at three different levels. This study was focused on the nanocomposite C and its base resin D. Additionally, some specific trials were conducted to obtain higher weight reduction parts and solid parts for the purpose of property comparison.

Techniques

The molded parts (standard dog-bone tensile testing bars and straight impact testing bars) were subjected to tensile testing, impact testing, following ASTM-D-638-02 and ASTM-D-256-02 standards, respectively. The samples were also examined by Scanning Electron Microscopy (JEOL SEM with accelerating voltage of 20 kV), Transmission Electron Microscopy (JOEL JEM100CX TEM), Dynamic Mechanical Analysis (DMA, Rheometrics DMTA-V), and X-ray Diffraction analysis (XRD, STOE high resolution X-ray diffractometer with Cu Kα radiation at 40 kV and 25 mA). SEM samples, TEM samples, and DMA samples were taken from the middle of the molded dog-bone bar. The SEM samples were characterized both in the melt flow direction and along the direction normal to the melt flow. The XRD samples were made by cutting and fine polishing the dog-bone in the middle plane in the thickness direction. Additional SEM micrographs were taken of tensile testing fracture surfaces.

Results and Discussion

The SEM results of microcellular structure are exemplified in Figures 1 through 9. Micrographs in Figures 1 through 4 were taken at the centers of samples.

*To whom correspondence should be addressed.

Figures 1 and 2 present the difference in cell structure between the microcellular nanocomposite, C, and its base resin, D, microcellular samples under the same molding condition. Nanocomposite has relatively smoother cell wall whereas its base resin has rougher wall surface. It implies that the nanoclay affects the cell formation and structure directly. Figures 1 and 3 show the comparison of microcellular structures between samples of same nanocomposite under different operation conditions. Even with the same amount of SCF addition, Trial C9 gave over 5-fold finer cells than Trial C3. Its cell density is about 150 times higher than that of the latter. In this case, high melt temperature and small shot size contribute to finer microcells.

Comparison between Figures 3 and 4 presents some controlled nucleation and growth of microcells with the nanocomposite as compared to its base resin. Microcells with smoother wall surface observed in the nanocomposite parts were normally smaller than those in the base resin parts. The experiments do show a slightly better control over the cell size at increased gas concentrations, possibly and partially because of a more highly dispersed nano-clay phase in the polymer/gas matrix. This is supported by TEM and XRD results. Figure 4 also indicates that the processing condition can improve the cell wall surface quality of the base resin. As the weight reduction of part increases, the heterogeneous cell growth and formation of base resin becomes more obvious as shown in Figure 4.

For base resin under different experimental conditions, the micrographs taken at the ends of sample cross-sections, as shown in Figure 5 and 6, show that the processing conditions also have some influence on the cell structure. It is understandable because nucleation and growth of cells are directly affected by the processing conditions such as melt temperature and injection pressure and pressure drop rate.

The micrographs in both Figures 7 and 8 show the entire sample cross-sections. It was verified that the solid boundary layer of microcellular nanocomposite part presents little structural difference from its fully solid counterparts. However, the gradual cell structural variation can be clearly seen from the surface layer to the center of part in the direction normal to the melt flow direction (Figure 7). However, it is usual to see variation in cell structure and cell distribution across the part thickness along the melt flow direction. Elongated microcells are visible in the vicinity of surface layer due to the fountain flow and the shear force (Figure 8), while uniform round shape cells occur in the center. The same trend was seen in the base resin microcellular parts.

At high weight reductions, even with the presence of nano-particles in microcellular parts, it was observed that the cell coalescence may take place, and some open cells can be formed under higher weight reduction conditions. It is also normal to see the irregular cell structure and cell distribution when the part weight reduction is high. The big voids can be easily found when the weight reduction of parts increases.

The fractographs of microcellular nanocomposite tensile testing bars are shown in Figure 10 (taken at a quarter length to the edge). Combining with Figure 12, it can be seen that the operation conditions affect significantly the fracture behaviors of microcellular nanocomposite. Based on the textures at the fractured surfaces, the molded parts under different process conditions exhibit a somewhat brittle, ductile, or hybrid fracture behavior. Samples of Trial 1 in Table 1 (low melt temperature and shot size) have certain 'brittle' fractured structure across the entire cross-section. On the other hand, samples of Trial 7 (high melt temperature and shot size) exhibit a much more ductile and heavily stretched fracture surface through the whole cross-section. Samples of Trial 4 (median melt temperature and shot size), however, have a transition from ductile to brittle structure from the sides to the center.

The results of mechanical property testing are tabulated in Table 2, and plotted in Figures 11, 12, and 13. As expected, the finer and denser microcells in the part usually lead to higher impact strength and less reduction in tensile strength, unless some defects such as coalescence and open cell occur in the cell formation. The stress vs. strain curves of base resin microcellular part, microcellular nanocomposite part, and their solid counterparts, are displayed in Figure 11. Both the solid base resin parts and the solid nanocomposite parts are all very ductile. The tensile modulus of microcellular nanocomposite part is usually higher than that of its corresponding base resin microcellular part. It should be noted that the ductility of microcellular nanocomposite depends on the processing conditions, as shown in Figure 12. From Table 2, it can be seen that the microcellular nanocomposite parts have smaller cell sizes and much higher cell densities under the same molding conditions than the base resin microcellular parts. This phenomenon was also observed for the other two kinds of nanocomposites. Under the similar molding process conditions, the differences in mechanical properties of different microcellular nanocomposite parts (A, E, C) are presented in Figure 13.

Some XRD results are depicted in Figures 15 and 16, in which p represents the direction parallel to the flow direction and r represents the direction normal to the flow direction. In the XRD tests, each sample was scanned in both directions. Figure 15 shows the difference in these two directions for nanocomposite A. The difference for nanocomposite C is shown in Figure 16. As evidenced in Figures 15 and 16, some clay decks or tactoids still exist and orientate in the melt flow direction. Those clay decks or tactoids behave as the normal fillers in terms of flow and orientation. Across the flow direction, the clay is highly dispersed. The disappearance of the 3.343 nm peak in microcellular nanocomposite part indicates that SCF helps to further exfoliate and uniformly disperse the clay during the course of melt processing. The nanoclay dispersion was also confirmed by the TEM micrograph (Figure 9).

Dynamic rheological study is of special interests, because the bulk properties of the microcellular nanocomposite depend not only on the bulk properties of the matrix, but also on the size and spacing of the cells as well as the physical and chemical properties of the nano-

fillers in the matrix. Some results in studying foams with DMA have been reported [4]. But the issues in microcellular nanocomposite are far more complicated because of the additional interfacial phenomena introduced with the clay/polymer/cell structure. The preliminary results in this study are shown in Figure 14. It can be seen that the elastic modulus of the base polyamide microcellular part and the microcellular nanocomposite part follow the patterns of their corresponding solid parts, respectively. The elastic modulus of base resin microcellular part is smaller in magnitude than that of microcellular nanocomposite part. However, the glass transition temperatures of these materials do not change too much. The phase angle curves for the nanocomposite and the microcellular nanocomposite parts are flatter than those of the solid base resin parts and microcellular parts.

Conclusions

Microcellular nanocomposite presents a new research area with numerous potential applications. Polyamide nanocomposites have been employed in microcellular injection molding to achieve small, uniform cell size and high cell density. Effects of processing conditions on the mechanical properties and microstructure have been studied. Both nano-clay and processing conditions have strong influence on cell structures and part properties. Microcellular nanocomposite can exhibit a behavior more or less ductile depending on the processing conditions. Supercritical fluid in microcellular injection molding facilitates the exfoliation of nanoclay in nanocomposite parts.

Acknowledgements

The materials used in the study were generously donated by the RTP Company. Part of this research is supported by the National Science Foundation (DMI-0140396). Some experimental assistance from Hrishikesh Kharbas and Paul Nelson is acknowledged.

References

[1] Wang, H., Zeng, C. C., Elkovitch, M., Lee, L. J., Koelling, K. W., *Polym. Eng. & Sci.*, 41, 11, 2036-2046 (2001).
[2] Svoboda, P., Zeng, C., Wang, H., Yang, Y., Li, H., Lee, L. J., and Tomasko, D., *2002 NSF DMII Grantee and Research Conference*, San Juan, Puerto Rico, January 7-10 (2002).
[3] Zeng, C., Han, X., Lee, L. J., Koelling, K. W., and Tomasko, D.L., ANTEC'2002.
[4] C. W. Macosko, *NATAS Proceedings*, 18, 271, 1989.

Table 1 L9 fractional orthogonal experimental design with polyamide nanocomposite C and base polyamide D

Trial for C, Trial for D	Melt Temperature (F)	Supercritical Content (wt%)	Shot Size (mm)	Injection Speed (%)	S/N Ratio for Trial C
1	450	0.2	16.5	20	35.12
2	450	0.4	18.4	40	35.98
3	450	0.6	20.5	60	36.74
4	*470*	*0.2*	*18.4*	*60*	*35.81*
5	*470*	*0.4*	*20.5*	*20*	*36.72*
6	470	0.6	16.5	40	35.01
7	*490*	*0.2*	*20.5*	*40*	*36.5*
8	490	0.4	16.5	60	35
9	490	0.6	18.4	20	36.07

Table 2 Morphological and mechanical properties of polyamide microcellular nanocomposite parts C vs. polyamide microcellular parts D

Trial for C, Trial for D	Weight reduction (%)		Cell size (microns)		Cell densities (No. per cubic-mm)		Impact Strength (Joules)		Tensile Strength (MPa)	
	C	D	C	D	C	D	C	D	C	D
1	18.0	8.8	10.42	28.72	408220	24570	0.113	0.172	57.03	36.70
2	8.0	7.4	9.11	53.15	619660	5910	0.0963	0.168	62.96	57.77
3	3.4	4.9	55.63	58.25	3570	3840	0.104	0.164	68.68	61.88
4	8.0	7.4	10.17	59.63	410440	3270	0.105	0.153	61.73	56.48
5	3.4	5.4	33.68	38.64	12980	10560	0.0881	0.183	68.58	59.03
6	13.1	8.8	13.85	72.24	238240	1450	0.115	0.166	56.28	53.60
7	8.0	6.4	31.24	59.32	16540	2460	0.113	0.180	66.83	56.35
8	12.1	8.8	13.80	33.36	201650	15340	0.109	0.153	56.27	54.61
9	7.3	7.8	9.97	41.02	530320	6390	0.104	0.156	63.58	55.88

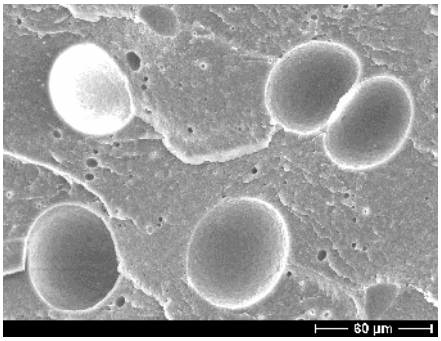

Figure 1 SEM micrograph of cells along the melt flow direction (Sample C3)

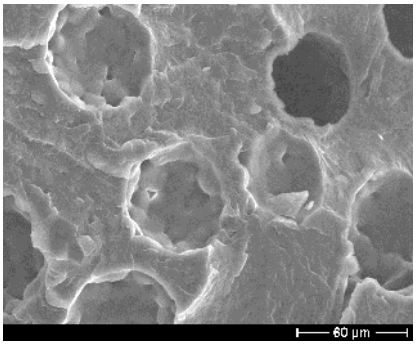

Figure 2 SEM micrograph of cells along the melt flow direction (Sample D3)

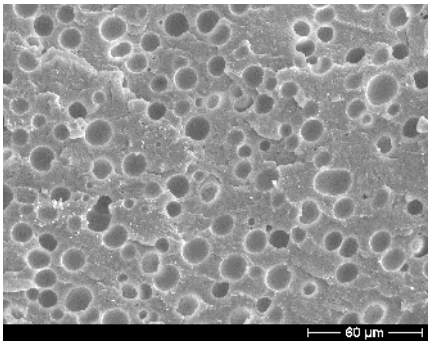

Figure 3 SEM micrograph of cells along the melt flow direction (Sample C9)

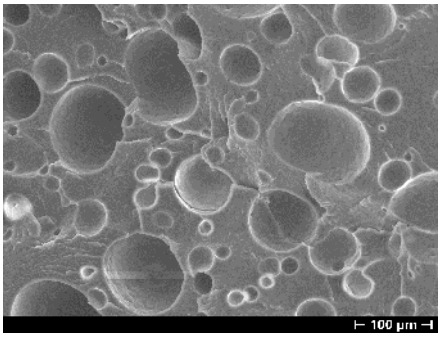

Figure 4 SEM micrograph of cells along the melt flow direction (Sample D9)

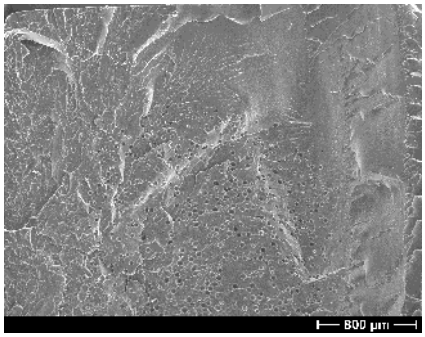

Figure 5 SEM micrograph of cells perpendicular to the flow direction (D5)

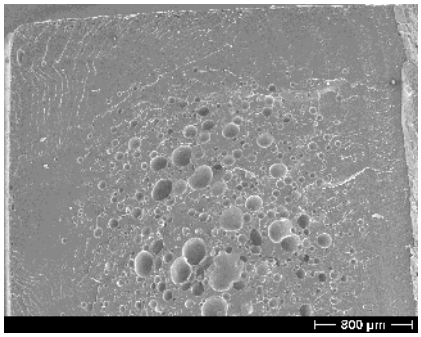

Figure 6 SEM micrograph of cells perpendicular to the flow direction (D9)

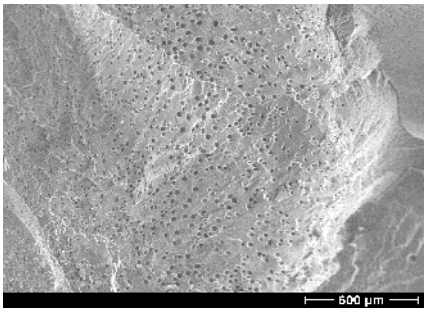

Figure 7 SEM micrograph of cells perpendicular to the flow direction (C5)

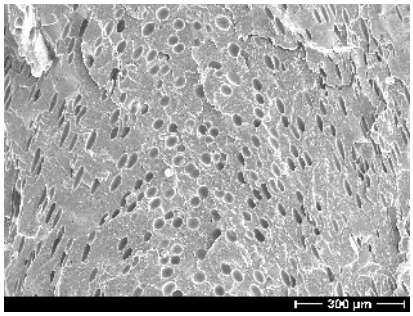

Figure 8 SEM micrograph of deformed cells along the melt flow direction (C5)

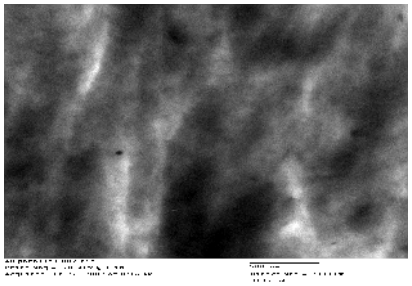

Figure 9 TEM micrograph of microcellular nanocomposite (Sample A8)

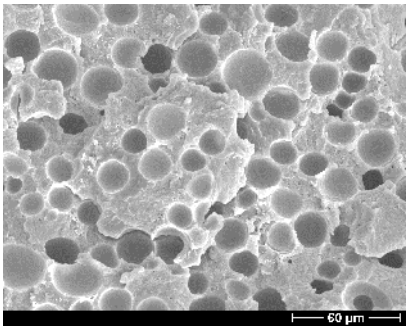

(a)

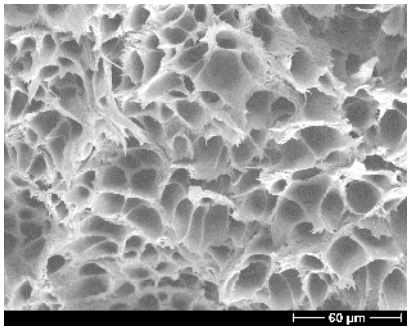

(b)

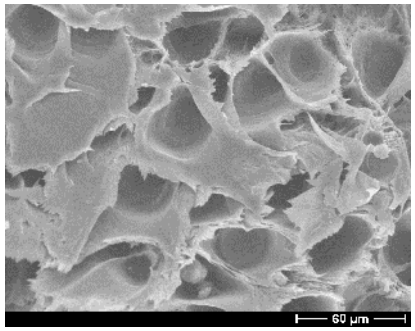

(c)

Figure 10 Fractographs of microcellular nanocomposites (a: Sample C1, b: Sample C4, c: Sample C7)

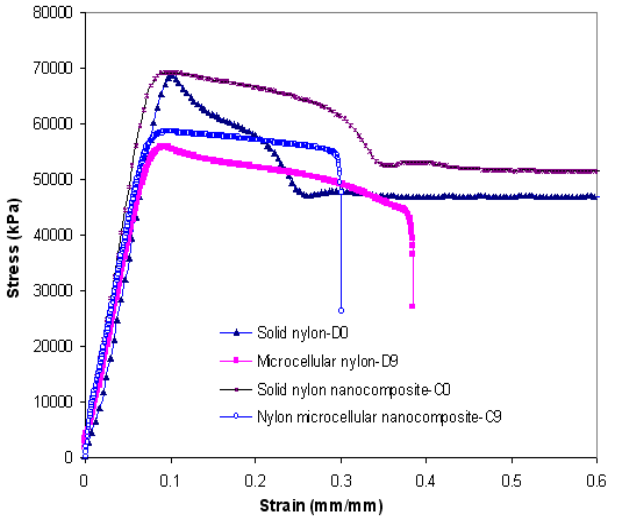

Figure 11 Tensile testing of microcellular nanocomposite C

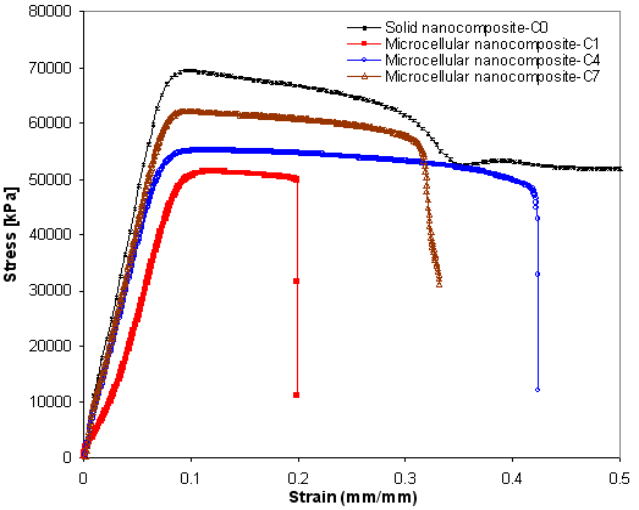

Figure 12 Tensile testing of microcellular nanocomposite C

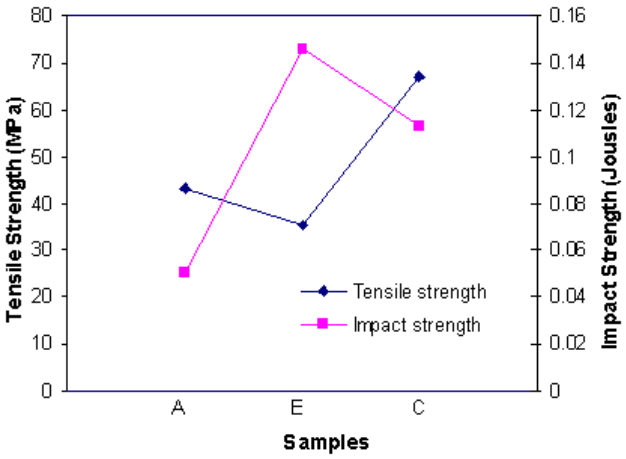

Figure 13 Comparison of mechanical properties for microcellular nanocomposites (A, C, E)

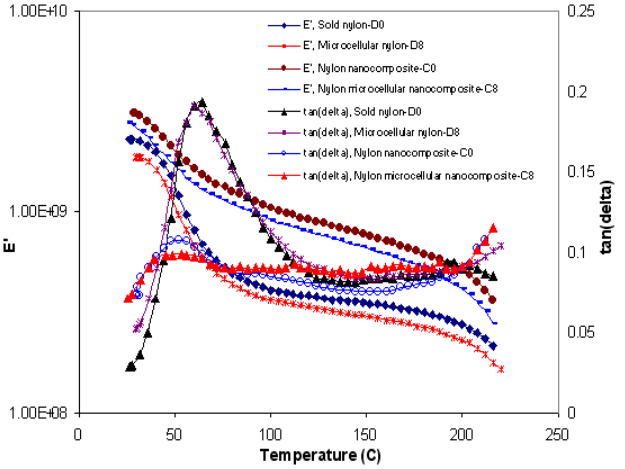

Figure 14 DMA of microcellular nanocomposites (C0, C8, D0, D8)

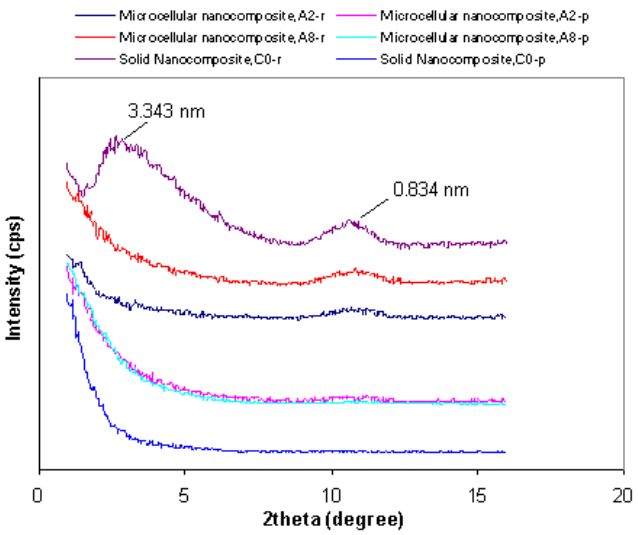

Figure 15 XRD of microcellular nanocomposites (C0, A2, A8)

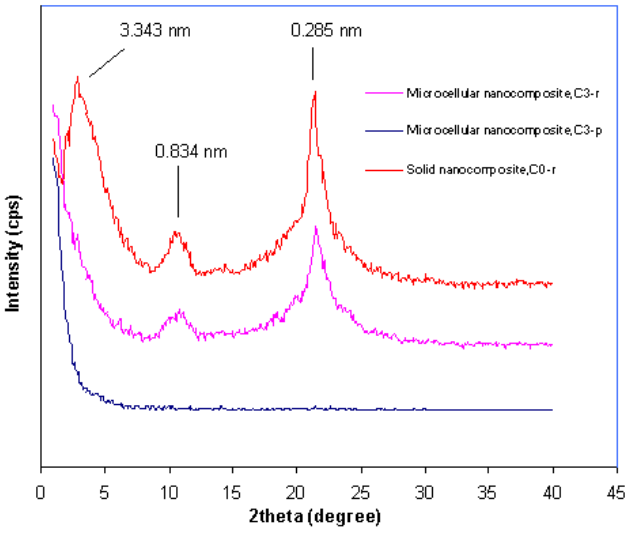

Figure 16 XRD of microcellular nanocomposites (C0, C3)